

Supplementary Information

Exploiting thiolate/disulfide redox couples toward large-scale electrochemical carbon dioxide capture and release

Xiaoxin Li¹, Chao Deng¹, Rong Chen¹, Xu Li¹, Furong Xie¹, Zinan Wu¹, Yu Xie²,
Song Wang³, Guo-Ming Weng^{1,*}

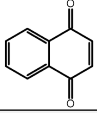
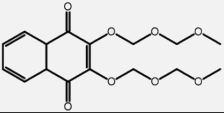
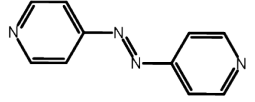
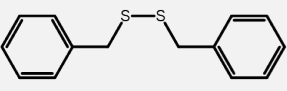
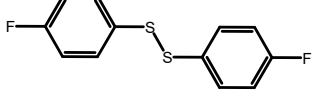
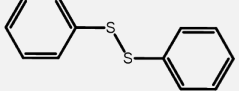
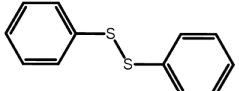
¹ Shanghai Key Laboratory of Hydrogen Science & Center of Hydrogen Science,
School of Materials Science and Engineering, Shanghai Jiao Tong University, Shanghai
200240 P. R. China

² Key Laboratory of Material Simulation Methods & Software of Ministry of Education,
Key Laboratory of Physics and Technology for Advanced Batteries of Ministry of
Education, College of Physics, Jilin University, Changchun 130012 P. R. China

³ Institute of Theoretical Chemistry, College of Chemistry, Jilin University, Changchun
130023 P. R. China

* Email: guoming.weng@sjtu.edu.cn

Table S1. Solubility of reported redox-active molecules for ECCR.

molecule	Structure	Solubility (M)	Solvent	Ref.
1,4-NQ		0.56	[emim][tcm]	1
LQ		Completely	Diglyme	2
AzPy		0.59 M	DMSO with 0.5M LiTFSI	3
BDS		2 M	DMF	4
FDS		Completely	DMF	This work
PDS		5.0 M	DMF	This work
PDS		3.5 M	DMF with 0.5 M NaTFSI	This work

Notes:

LQ and FDS are liquid. Therefore, they are miscible with aprotic solvent.

Abbreviations of molecule in Table S1.

1,4-NQ: 1,4-naphthoquinone

[emim][tcm]: 1-ethyl-3-methylimidazolium tricyanomethanide

LQ: 2,3-Di-(2-(2-methoxyethoxy)ethoxy)-1,4-naphthoquinone

AzPy: Azopyridine

DMSO: Dimethyl sulfoxide

LiTFSI: Lithium bis(trifluoromethanesulphonyl)imide

BDS: Benzyl disulfide

FDS: 4-fluorophenyl disulfide

DMF: N, N-dimethyl formamide

PDS: Phenyl disulfide

NaTFSI: Sodium bis(trifluoromethanesulphonyl)imide

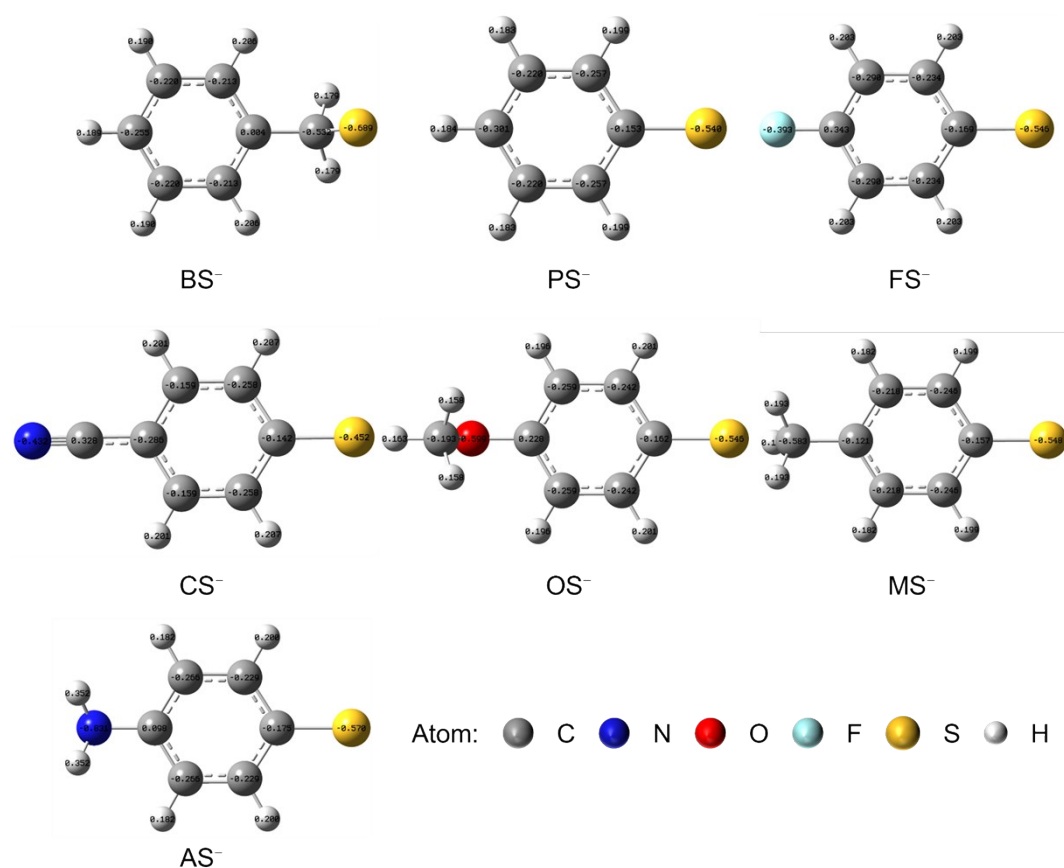


Figure S1. The Natural Population Analysis (NPA) charges. The NPA charges of different thiolate anion, obtained from Nature Bond Orbitals (NBO). **BS⁻**: benzyl thiolate, **PS⁻**: phenyl disulfide, **OS⁻**: 4-methoxyphenyl thiolate, **MS⁻**: 4-methylphenyl thiolate, **AS⁻**: 4-aminodiphenyl thiolate, **FS⁻**: 4-fluorophenyl thiolate, **CS⁻**: 4-cyanophenyl thiolate.

The NPA charges of S atom in **PS⁻** are -0.540, which is less than that of **BS⁻** (-0.689). After substituting the H atom by electron-donating groups, the NPA charges of S atom increase. While the H is substituted by electron-withdrawing group, the NPA charges of S atom decrease.

Table S2. Summary of NPA charges of S atom in Figure S1 for different thiolate anions.

S atom in thiolate anion	NPA charges
BS⁻	-0.689
PS⁻	-0.540
MS⁻	-0.548
OS⁻	-0.546
AS⁻	-0.570
FS⁻	-0.546
CS⁻	-0.452

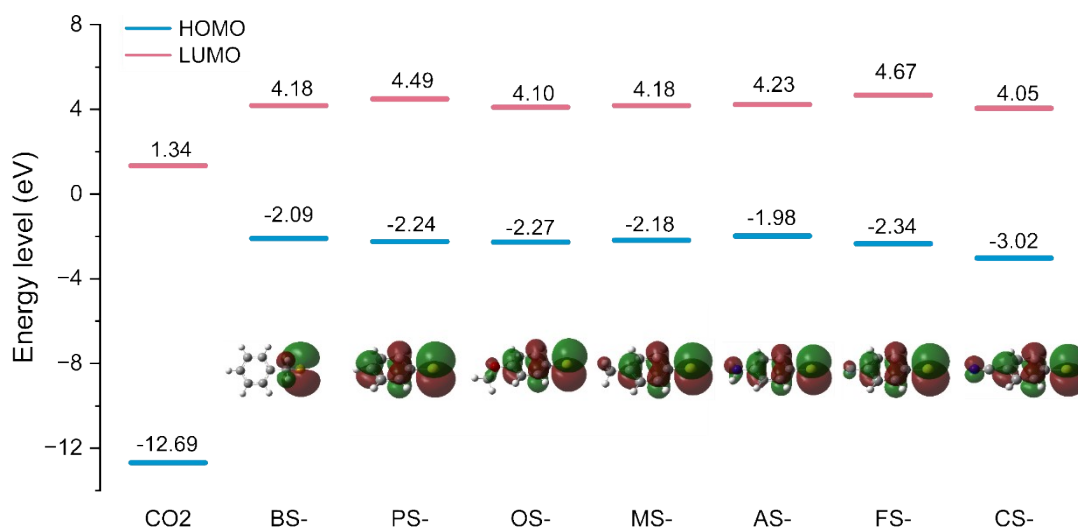


Figure S2. HOMO and LUMO energy level diagram. Visualized HOMO and LUMO distributions and corresponding energy values of CO₂ and different thiolate anions. The LUMO energy of CO₂ here is positive, while the widely acceptance value should be negative.⁵ When B3LYP/6-311+G(d, p) was used to perform the calculation, the negative energy of CO₂ LUMO (-0.54 eV) was obtained. Although the B3LYP functional is suitable for small molecule CO₂, the ω B97XD functional with van der Waals corrections is more suitable for investigated disulfides with π system. Therefore, we proceeded all calculation by using ω B97XD functional, in order to maintain consistency in the used functional.

Table S3. Summary of HOMO-LUMO gap between thiolate anions and CO₂, as well as the binding energy of corresponding CO₂ adducts.

Thiolate anion	HOMO-LUMO gap (eV)	Binding energy to CO ₂ (ΔH , kJ mol ⁻¹)
BS ⁻	3.43	-71.09
PS ⁻	3.58	-27.62
MS ⁻	3.52	-29.26
OS ⁻	3.61	-35.94
AS ⁻	3.32	-25.27
FS ⁻	3.68	-20.58
CS ⁻	4.36	-17.26

Note: more DFT calculation details are shown in **Supplementary Note 2**.

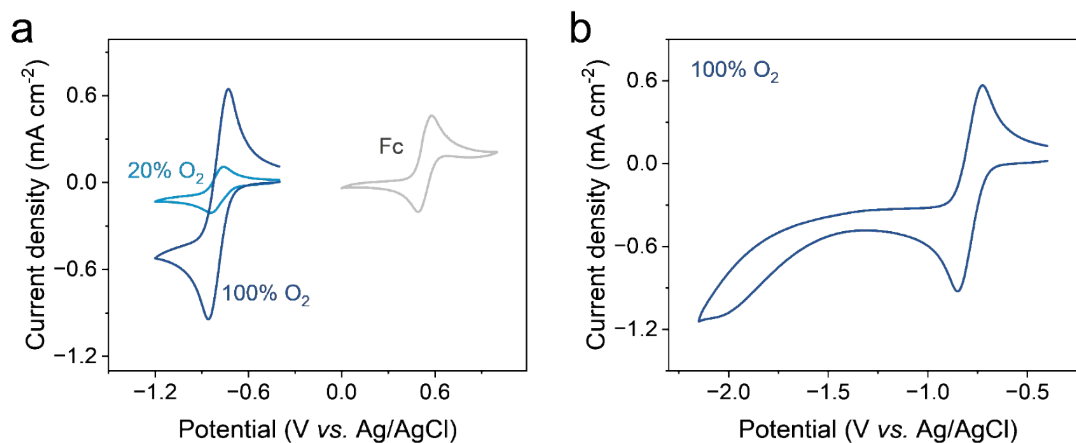


Figure S3. (a) CV of 20%, 100% O₂ (pale blue, dark blue curves) and 5 mM ferrocene (gray curve) at a measuring window of -0.4 ~ -1.2 V and 1 ~ 0 V, respectively. (b) CV of 100% O₂ at a measuring window of -0.4 ~ -2.15 V. The cyclic voltammograms were collected in DMF with 0.1 M TBAP as the supporting electrolyte at a scan rate of 10 mV s⁻¹. The O₂ was firstly reduced to O₂^{•-} at around -0.8 V, and the O₂^{•-} was further reduced to O₂²⁻ when the applied potential increase to -2.0 V.⁶

Table S4. Half wave potential ($E_{1/2}$) of O₂/O₂^{•-} versus different reference electrodes.

Reference \ Species	$E_{1/2}$ (V) for 20% O ₂	$E_{1/2}$ (V) for 100% O ₂	$E_{1/2}$ (V) for ferrocene
Ag/AgCl	-0.800	-0.793	0.535
SCE	-0.844	-0.837	0.491
Fc ⁺ /Fc	-1.335	-1.328	0

Notes: For the readers' information, a derivate of naphthoquinone with liquid phase reported by Diederichsen et al. exhibits a more positive reduction potential than that of O₂/O₂^{•-} (~ -1.2 V vs. Fc⁺/Fc) in aprotic solution under room temperature.²

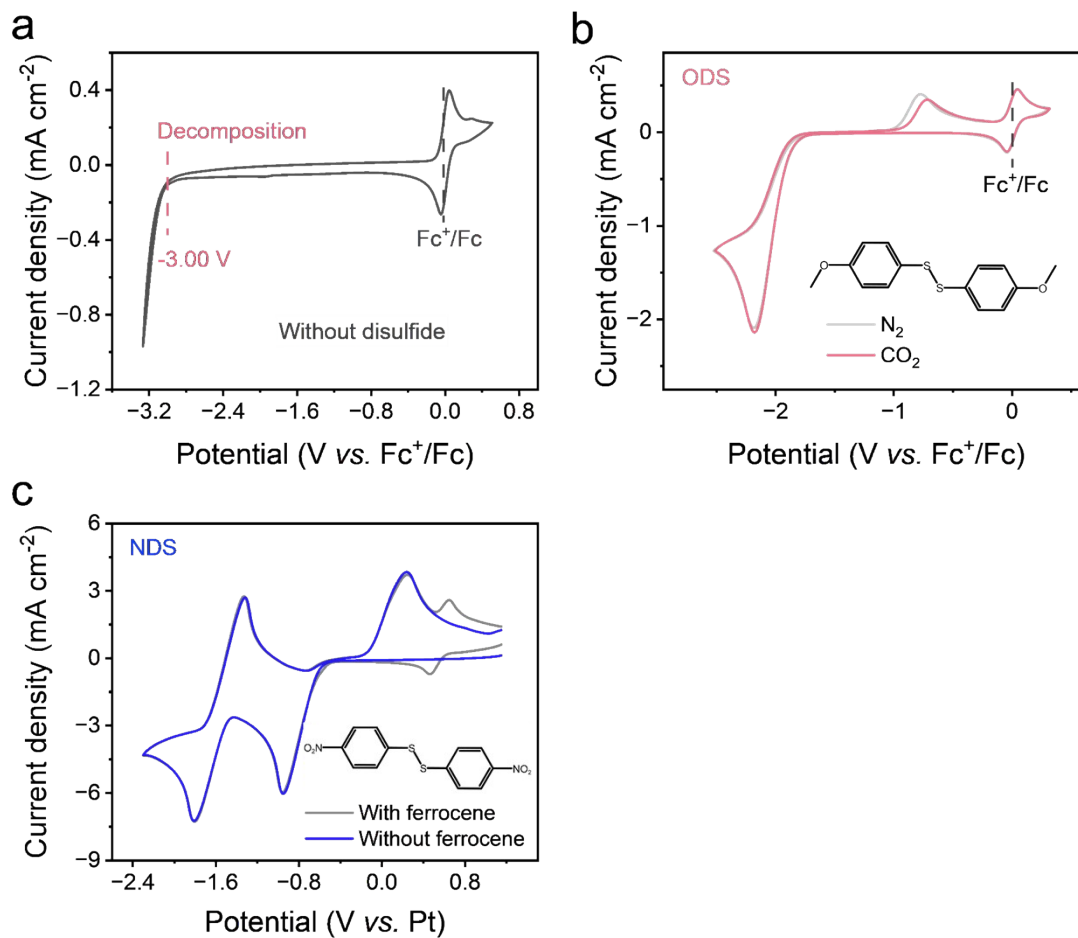


Figure S4. (a) cyclic voltammogram for electrochemical stability of electrolyte. The CV was performed under N_2 without disulfide in the electrolyte. The electrolyte started to decompose at around -3.00 V. (b) Cyclic voltammograms of 20 mM 4-methoxyphenyl disulfide (ODS) under N_2/CO_2 with 5 mM ferrocene at scan rate of 10 mV s^{-1} (c) Cyclic voltammograms of 20 mM 4-nitrophenyl disulfide (NDS) under N_2 with/without 5 mM ferrocene at scan rate of 100 mV s^{-1} .

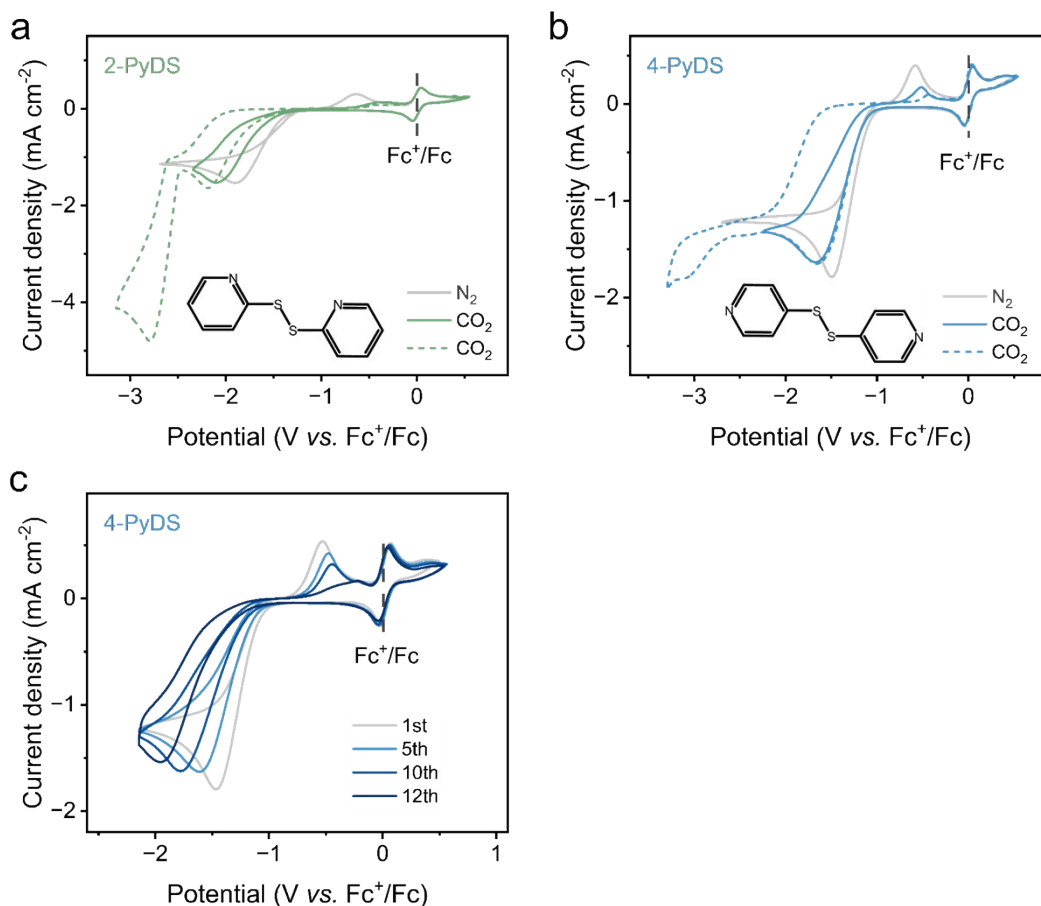


Figure S5. Cyclic voltammetry of 2-PyDS and 4-PyDS. (a) and (b) are the Cyclic voltammograms of 20mM 2,2'-dipyridinyl disulfide (2-PyDS) and 4,4'-dipyridinyl disulfide (4-PyDS) in DMF with 0.1 M TBAP, respectively, under N₂ and CO₂. As shown by dash line, there is one more reduction peak when the scan window was extended. This should result from the reduction of pyridine-N after forming CO₂ adducts. (c) CV curves of 4-PyDS at different cycle number under N₂ atmosphere. The CV curve can't overlap with each other, which should result from the unstability of dipyridine disulfide.^{7, 8}

Table S5. Peak potential of 2-PyDS and 4-PyDS.

Molecule	Condition	E _{pc} (V vs. Fc ^{+/Fc})	E _{pa} (V vs. Fc ^{+/Fc})	ΔE _{pa} =E _{pa} (CO ₂) - E _{pa} (N ₂)
2,2'-dipyridinyl disulfide (2-PyDS)	N ₂	-1.905	-0.634	0.283
	CO ₂	-2.096	-0.351	
4,4'-dipyridinyl disulfide (4-PyDS)	N ₂	-1.496	-0.582	0.067
	CO ₂	-1.676	-0.515	

Table S6. Peak potential, ΔE_{cell} and ΔG for PDS, FDS and CDS with either 0.1 M LiTFSI or NaTFSI as the supporting electrolyte.

Molecule	Condition	E_{pc} (V)	E_{pa} (V)	ΔE_{cell} (V)	ΔG $\text{kJ mol}^{-1} \text{CO}_2$	ΔE_{pa} (V)
PDS	Li ⁺ (N ₂)	-2.140	-0.742	-	-	0.428
	Li ⁺ (CO ₂)	-2.141	-0.314	1.827	176	
	Na ⁺ (N ₂)	-2.139	-0.732	-	-	0.282
	Na ⁺ (CO ₂)	-2.125	-0.450	1.675	162	
FDS	Li ⁺ (N ₂)	-2.002	-0.725	-	-	0.389
	Li ⁺ (CO ₂)	-2.037	-0.336	1.701	164	
	Na ⁺ (N ₂)	-2.002	-0.718	-	-	0.209
	Na ⁺ (CO ₂)	-2.016	-0.509	1.507	145	
CDS	Li ⁺ (N ₂)	-1.294	-0.668	-	-	0.022
	Li ⁺ (CO ₂)	-1.314	-0.646	0.668	64	
	Na ⁺ (N ₂)	-1.274	-0.695	-	-	0.022
	Na ⁺ (CO ₂)	-1.291	-0.673	0.618	60	

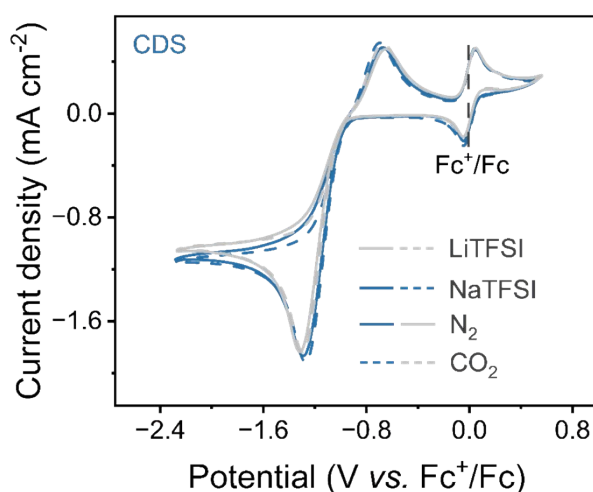


Figure S6. Cyclic voltammograms of 20 mM CDS with either 0.1 M LiTFSI (gray curves) or 0.1 M NaTFSI (dark blue curves) as the supporting electrolyte in DMF, under the atmosphere of N₂ (solid curves) and CO₂ (dash curves).

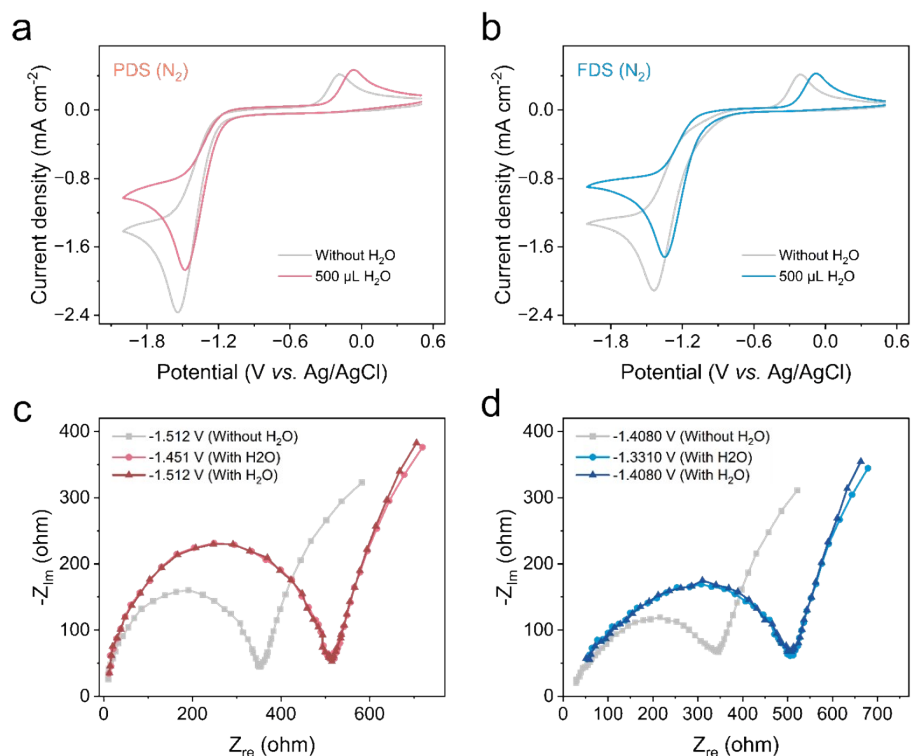


Figure S7. Cyclic voltammograms and electrochemical impedance spectroscopy (EIS) for the systems with PDS and FDS. CV of 20 mM PDS (a) and FDS (b) in 0.1 TBAP with/without H₂O under N₂. (c) and (d) are the EIS spectrum of the systems with PDS and FDS, respectively, with/without H₂O under different applied potential. Experimental details: working electrode, glass carbon; Counter electrode, Pt foil; reference, Ag/AgCl. Same rate for CV, 10 mV s⁻¹. Frequency range for EIS, 100 Hz to 1 MHz. The larger radius of EIS spectra, the larger charge transfer resistance. Note that the applied potentials for EIS were calculated by plus 30 mV with E_{pc}, and the E_{pc} was obtained from the corresponding CV curve.

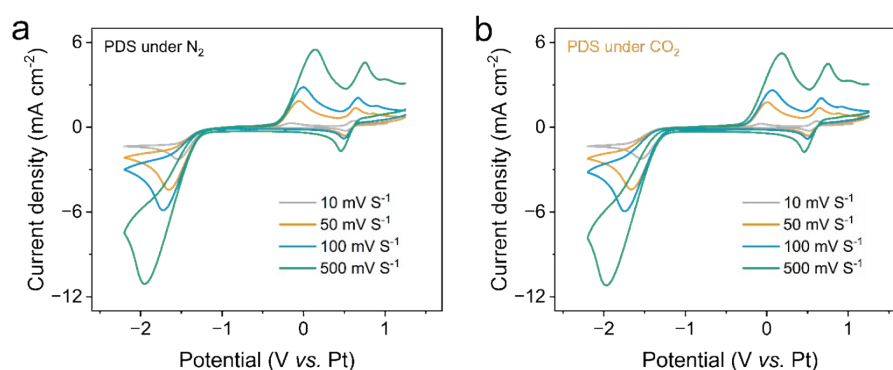


Figure S8. Cyclic voltammograms of the system with PDS at different scan rates. (a) and (b) are CV curves of 20 mM PDS under N₂ and CO₂, respectively. Information about the colorful labels and curves: 10 mV s⁻¹ (gray), 50 mV s⁻¹ (orange), 100 mV s⁻¹ (blue) and 500 mV s⁻¹ (green).

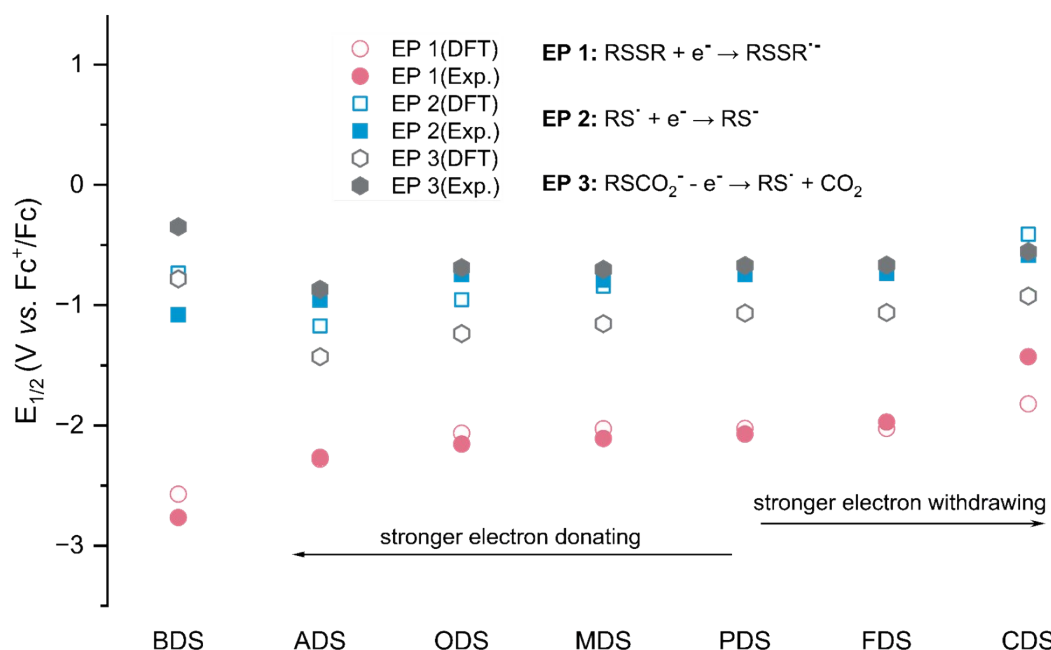


Figure S9. Comparison of the standard redox potential from DFT calculation and experiment results for different disulfides. The red circle, blue square and gray hexagon symbols represent the potential of electrochemical processes EP 1, EP 2 and EP 3, respectively, corresponding to **Figure 4** in main text. The filled and unfilled symbols represent the potential from experimental results and DFT calculation, respectively.

Table S7. Summary and comparison of the standard redox potential from DFT calculation and experiment results for different disulfides.

disulfide	EP 1 (V vs. Fc ⁺ /Fc)		EP 2 (V vs. Fc ⁺ /Fc)		EP 3 (V vs. Fc ⁺ /Fc)	
	DFT	Exp.	DFT	Exp.	DFT	Exp.
BDS	-2.571	-2.765	-0.732	-1.078	-0.781	-0.348
PDS	-2.025	-2.072	-0.728	-0.743	-1.066	-0.670
MDS	-2.027	-2.109	-0.841	-0.79	-1.154	-0.702
ODS	-2.064	-2.155	-0.954	-0.744	-1.236	-0.688
ADS	-2.280	-2.265	-1.172	-0.958	-1.428	-0.868
FDS	-2.025	-1.971	-0.718	-0.736	-1.061	-0.666
CDS	-1.821	-1.428	-0.410	-0.583	-0.924	-0.554

Note:

- (1) The details of DFT calculation method were shown in **supplementary note 2**.
- (2) The experimental redox potentials of the above disulfides were estimated by the equation $E_{1/2} = E_{pc} + 30 \text{ mV} = E_{pa} - 30 \text{ mV}$
- (3) The redox potentials of EP 1 and EP 2 processes obtained from DFT calculation match well the experimental results, while the redox potentials of EP 3 process have some deviation.

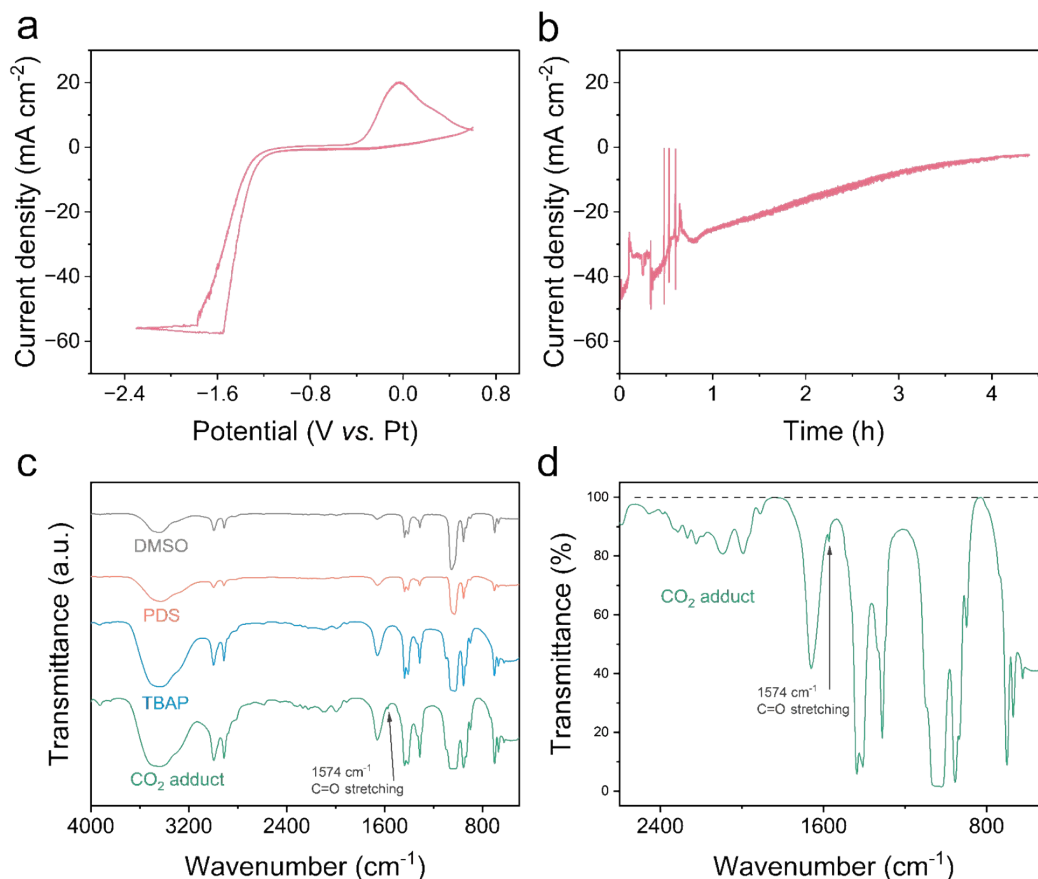


Figure S10. Identification of CO₂ adducts with Fourier transform infrared (FTIR) Spectrometry. (a) CV curve of 20 mM PDS in DMSO with 0.1M TBAP by using a H-cell with continuous CO₂ bubbling (10 mL min⁻¹). (b) Chronoamperometry curve (bulk electrolysis) at -1.8 V vs. Pt with continuous CO₂ bubbling at a flow rate of 10 mL min⁻¹. The fluctuation of i-t curve should result from the bubbling of CO₂. The color change is negligible and thus can't be observed, since the conjugated system of PS⁻ or PSCO₂⁻ is too small. (c) FTIR spectra for DMSO and solution of PDS, TBAP and CO₂ adducts (PSCO₂⁻) in DMSO. (d) The enlarged FTIR spectra of CO₂ adducts are to show that the C=O bond stretching vibration should not result from signal noise, because the signal noise can not reach about 85% transmittance. Note: The PSCO₂⁻ in catholyte was collected from bulk electrolysis in a H-Cell (details in **Electrochemical experiments** of main text). Then the catholyte was dropped on KBr single crystal wafer with a thickness of 1 mm, and formed a liquid layer between two KBr slices. After capturing CO₂, new absorption peak at 1574 cm⁻¹ appears, which could be assigned to C=O bond stretching vibration. Thus, the FTIR results confirmed the formation of CO₂ adducts, i.e., PSCO₂⁻.^{4,9}

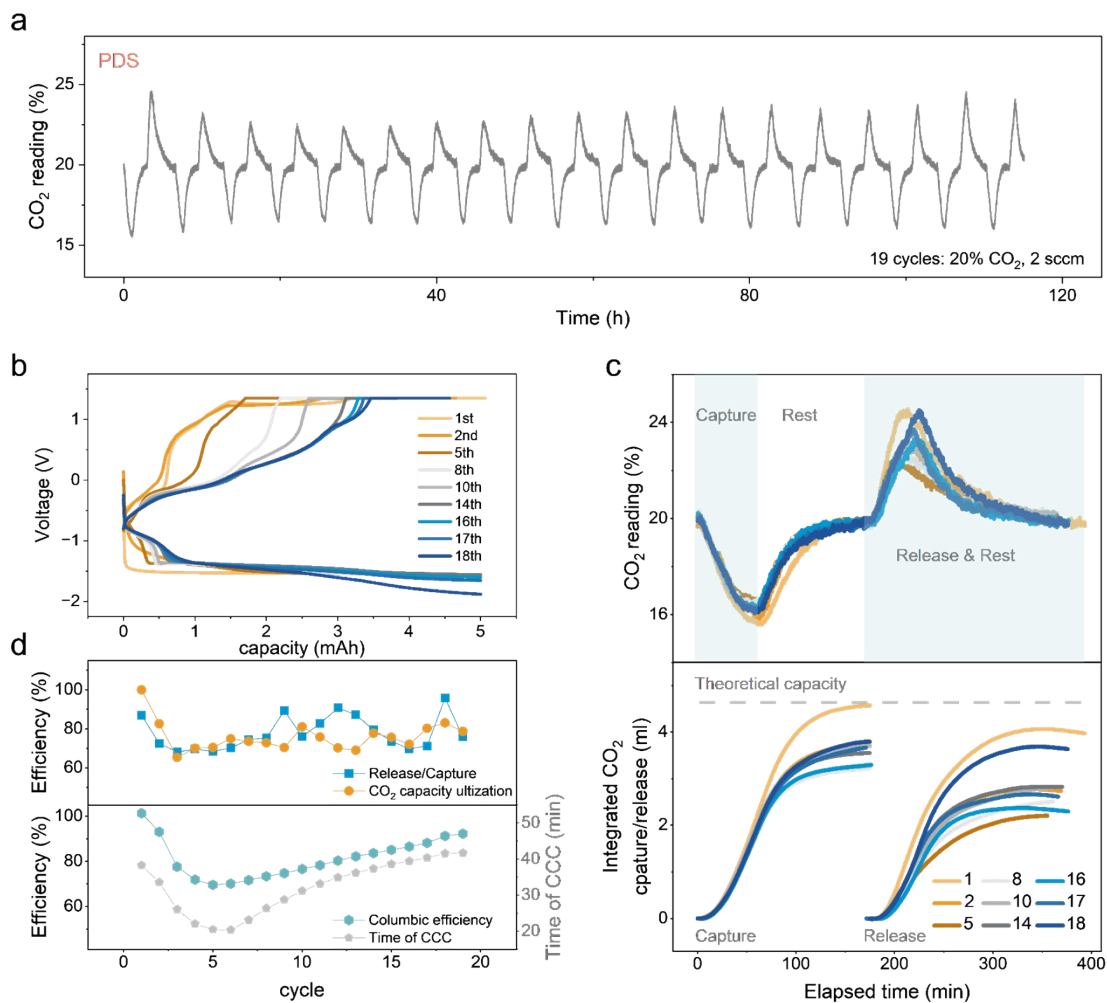


Figure S11. Performance of CO₂ capture and release cycles in a flow cell with PDS as the sorbent.

(a) CO₂ reading curve of 19 repeated capture and release cycles at the exit of PDS tank.

(b) The selected corresponding voltage-capacity curves.

(c) The top panel, CO₂ reading for selected capture and release cycles. The bottom panel, cumulative amount of captured and released CO₂ in selected cycles. For capture (discharge) process, the DS was reduced to react with CO₂ at 5 mA for 60 min and then rested for 115 min. For release (charge) process, CO₂ adducts were oxidized to release CO₂ and regenerate DS, at 5 mA to 1.35 V followed by a 100 min constant voltage of 1.35 V hold and a 60 min rest.

(d) Release/capture efficiency (blue square), CO₂ capacity utilization (yellow circle), columbic efficiency (green hexagon), and time of constant current charge (CCC) (gray pentagon) for 19 cycles shown in **(a)**. The CO₂ capacity utilization efficiency was about 100% in the first cycle, and then gradually decrease and hover around 75%. The release/capacity efficiency showed a trend of decrease firstly and then increase in cycles as columbic efficiency, and have an average efficiency of ~78%. In the 18th cycle, the release/capacity efficiency and columbic efficiency returned to ~96% and ~91%, respectively, suggesting the good stability and reversibility of the PDS in CO₂ capture-release cycle.

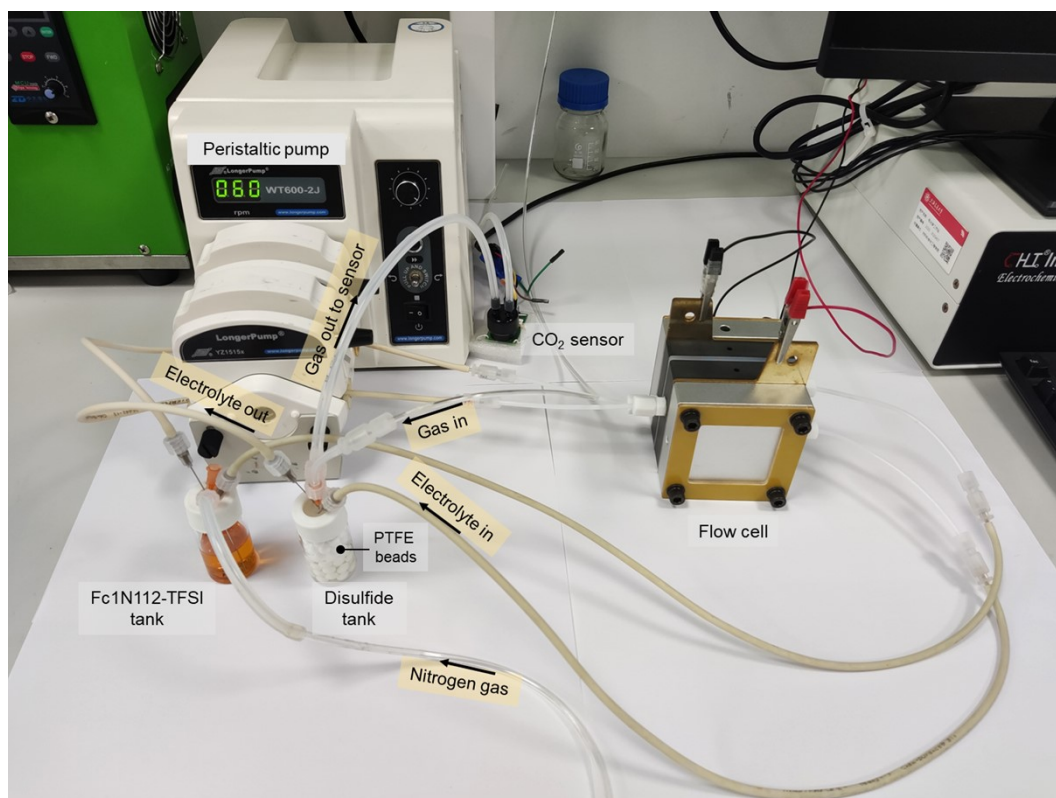


Figure S12. Flow system for CO₂ capture and release. The main part of the CO₂ capture and release system are shown in this photo. Noted that the durable peristaltic pump tubes (Chem-Duranc; Masterflex) and PTFE tubes ($\text{\O} = 3 \text{ mm}$) were used in our system, to avoid the undesirable corrosion of tube by organic electrolyte.

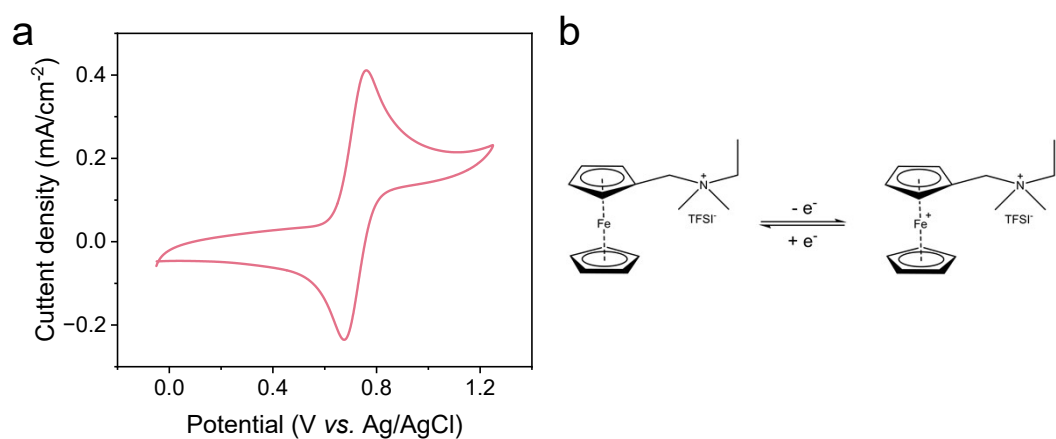


Figure S13. Redox-active substance as the counter electrolyte to balance the charge. (a) Cyclic voltammogram of Fc1N112-TFSI in DMF. In this test, 0.1 M TBAP and Ag/AgCl were used as the supporting electrolyte and the reference electrode, respectively. (b) Illustration of the redox reaction for Fc1N112-TFSI. This is also reported elsewhere.¹⁰

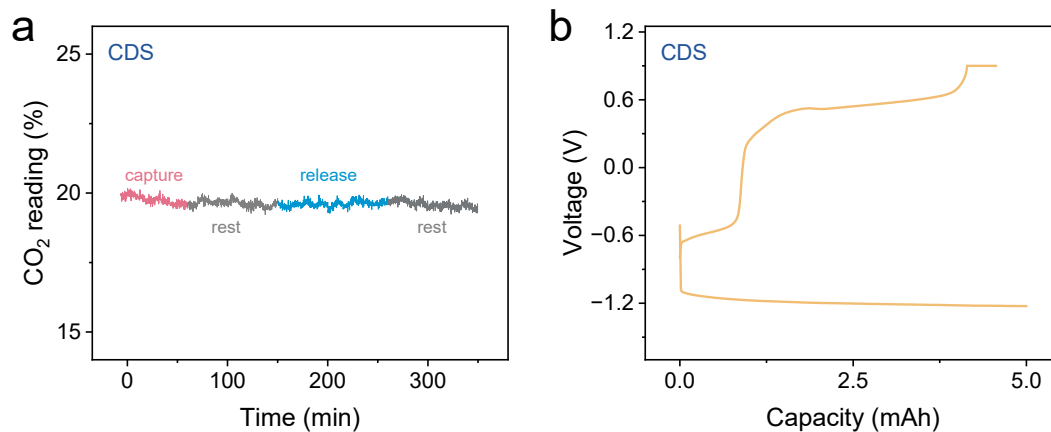


Figure S14. Electrochemical CO₂ capture and release using CDS as the sorbent. (a) CO₂ reading for one cycle using CDS. **(b)** The corresponding voltage-capacity curve. For CO₂ capture, the CDS was reduced at 5 mA for 60 min followed by 90 min rest. For CO₂ release, the adducts were oxidized at 5 mA to 0.9 V followed by 60 min constant voltage hold at 0.9 V, and then rested for another 90 min. The CO₂ reading curve did not show any change during discharge or charge process, which demonstrated again that the CDS with a stronger electron-withdrawing group could not capture CO₂.

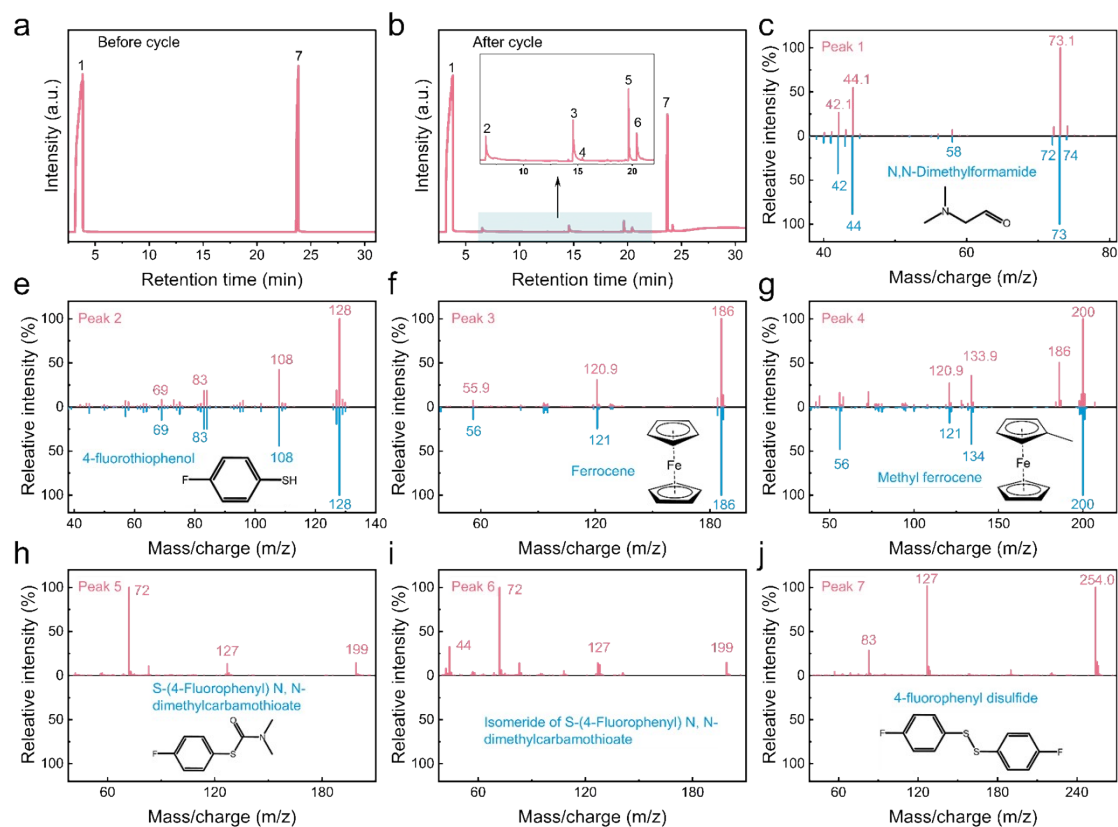


Figure S15. Gas Chromatography-Mass Spectrometer (GC-MS) for the electrolyte of the FDS tank before and after cycling. (a) and (b) are gas chromatograms for the electrolyte of the FDS tank before and after cycling, respectively. The appearance of ferrocene and its derivate after cycling indicated that the crossover phenomenon between the FDS and counter compartments. Moreover, some new peaks indicated the parasitic reaction could take place during the cycling experiment. (c), (d), (e), (f), (g), (h), (i) and (j) are standard (blue line) and experimental (red line) mass spectra for N, N-dimethylformamide, 4-fluorothiophenol, ferrocene, methyl ferrocene, S-(4-fluorophenyl) N, N-dimethylcarbamothioate, isomeride of S-(4-fluorophenyl) N, N-dimethylcarbamothioate (a tentative guess) and FDS, respectively, with the corresponding molecular structure at the bottom of the figure.

Note that (1) the standard mass spectra of S-(4-fluorophenyl) N, N-dimethylcarbamothioate and FDS are not included in the NIST mass spectral library; (2) the formation of a little amount of S-(4-fluorophenyl) N, N-dimethylcarbamothioate demonstrate the minor side reaction of FS^- with DMF; (3) the founding of Fc and it's derivates demonstrate the occurrence of crossover phenomenon.

Table S8. Identification of GC-MS shown in Figure S15 for electrolyte of FDS tank.

Peaks	Retention time (min)	Identification	Molecular weights
1	3.800	N, N-dimethylformamide	73
2	6.532	4-fluorothiophenol	128
3	14.566	Ferrocene	186
4	15.425	Methyl ferrocene	200
5	19.666	S-(4-fluorophenyl) N, N-dimethylcarbamothioate	199
6	20.423	Isomeride of S-(4-fluorophenyl) N, N-dimethylcarbamothioate (a tentative guess)	199
7	23.696	4-fluorophenyl disulfide	254

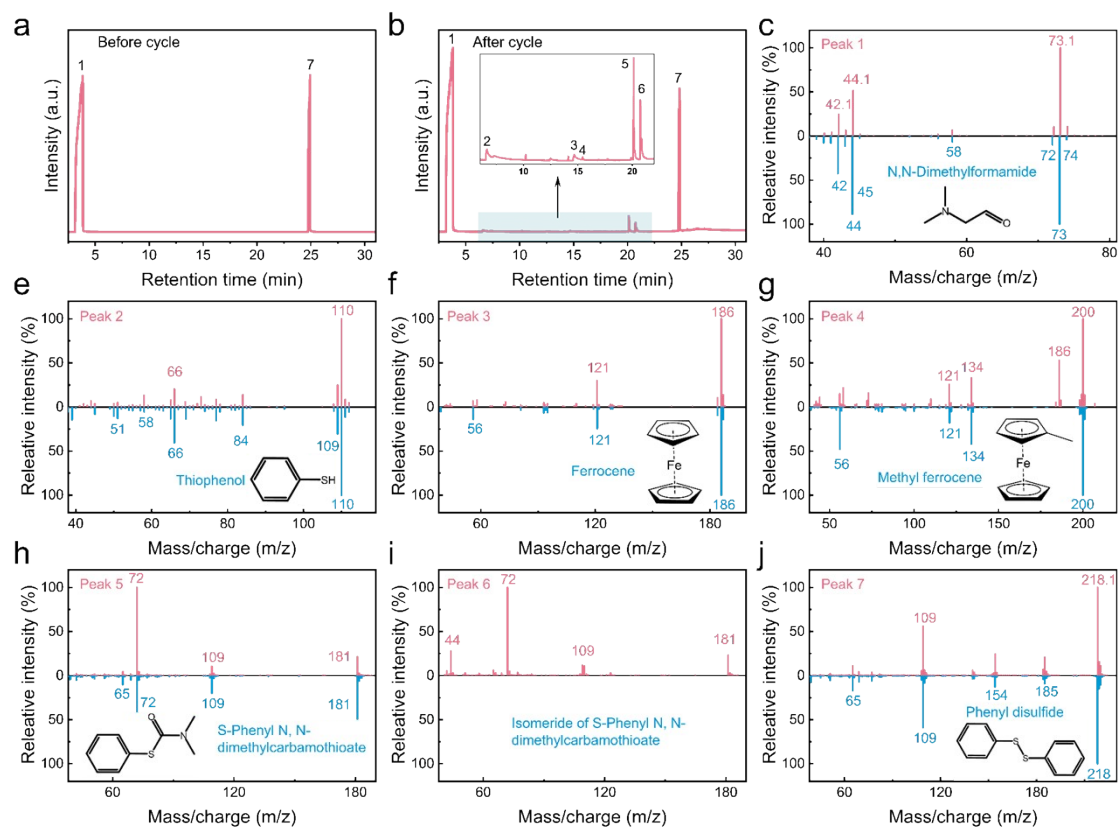


Figure S16. Gas Chromatography-Mass Spectrometer (GC-MS) for the electrolyte of the PDS tank before and after cycling.

(a) and (b) are gas chromatograms for the electrolyte of the PDS tank before and after cycling, respectively. The appearance of ferrocene and its derivatives after cycling indicated that the crossover phenomenon between the DS and counter chambers. Meanwhile, some new peaks indicated that parasitic reactions could occur during the cycling test. (c), (d), (e), (f), (g), (h), (i) and (j) are standard (blue line) and experimental (red line) mass spectra for N, N-dimethylformamide, thiophenol, ferrocene, methyl ferrocene, S-phenyl N, N-dimethylcarbamothioate, isomeride of S-phenyl N, N-dimethylcarbamothioate (a tentative guess) and PDS, respectively, with the corresponding molecular structures at the bottom of the figure.

Note that (1) the formation of a little amount of S-phenyl N, N-dimethylcarbamothioate demonstrates the existence of a minor side reaction of PS^- with DMF; (2) the finding of Fc and its derivatives demonstrate the occurrence of the crossover phenomenon.

Table S9. Identification of GC-MS presented in Figure S16 for electrolyte of PDS tank.

Peaks	Retention time (min)	Identification	Molecular weights
1	4.062	N, N-dimethylformamide	73
2	6.633	Thiophenol	110
3	14.672	Ferrocene	186
4	15.437	Methyl ferrocene	200
5	20.118	S-phenyl N, N-dimethylcarbamothioate	181
6	20.744	Isomeride of S-phenyl N, N-dimethylcarbamothioate (a tentative guess)	181
7	24.82	Phenyl disulfide	218

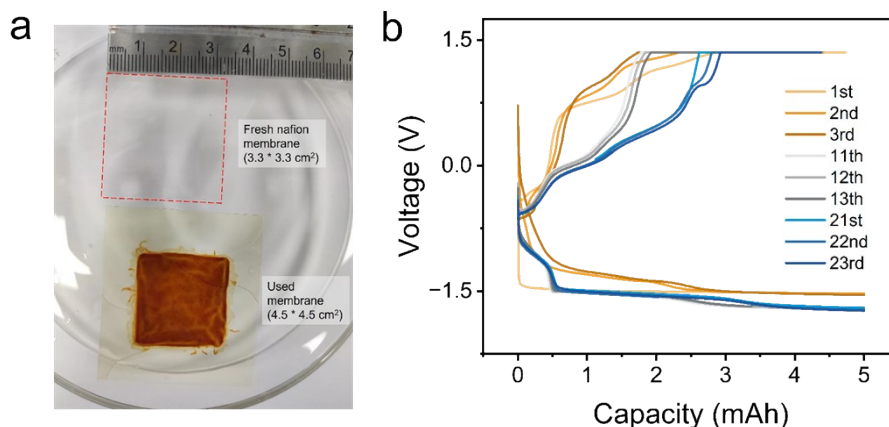


Figure S17. (a) A photograph showing a piece of fresh nafion membrane (3.3 * 3.3 cm²) and a piece of used nafion membrane (4.5 * 4.5 cm²). The expansion rate of the nafion membrane is about 186.0% after treatment, which could be the reason for crossover phenomenon of electrolytes. There were yellow substances absorbed on nafion membrane after use. The yellow substances might be the ferrocene derivatives absorbed on nafion membrane, and they could cause the increase of cell resistance during the cycling experiment. **(b)** The corresponding voltage-capacity curves of selected cycles. The applied voltage for constant current discharge (CCD) gradually increased after each cycle, which could be resulted from the increase of cell resistance, the crossover of electrolytes and the complicated parasitic reaction during cycling (**Figures S15 and S16**).

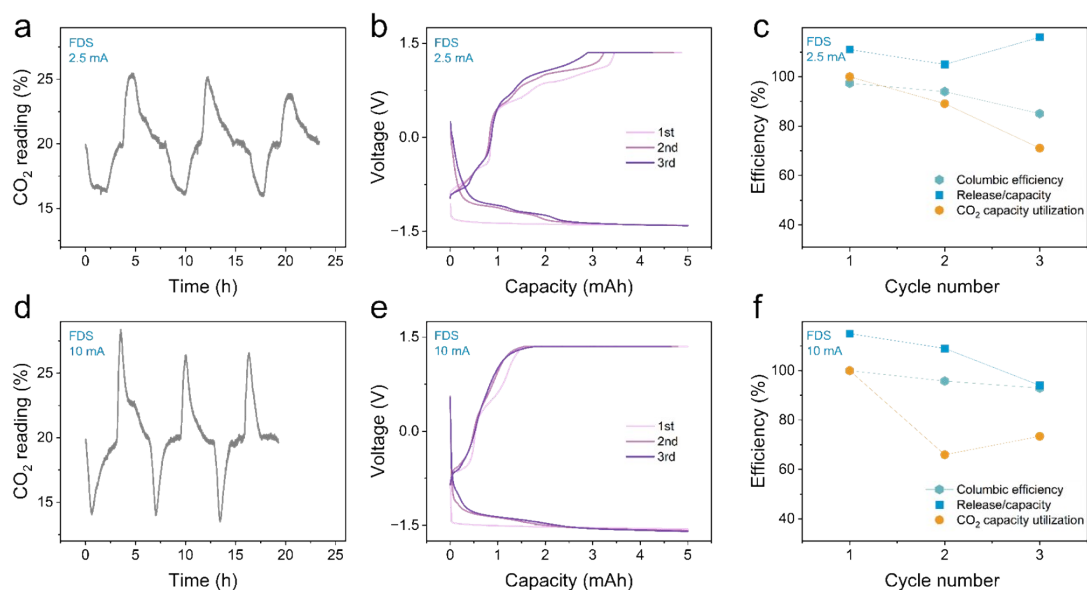


Figure S18. Performance of CO₂ capture and release cycles in a flow cell with FDS under different constant current discharge (CCD). (a) CO₂ readings curves at the gas outlet of FDS tank over 3 capture and release cycles at CCD of 2.5 mA. For capture (CCD) process, the FDS was reduced to react with CO₂ at 2.5 mA for 120 min and then rested for 90 min. For release (charge) process, CO₂ adducts (FSCO₂⁻) were oxidized to release CO₂ and regenerate FDS, at 5 mA to 1.35 V followed by a 100 min constant voltage of 1.35 V hold and an 80 min rest. (b) The voltage-capacity curves for capture-release cycles shown in (a). (c) Release/capture efficiency (blue square), CO₂ capacity utilization (yellow circle) and columbic efficiency (green hexagon) for 3 cycles shown in (a). (d) CO₂ readings curves at the gas outlet of FDS tank over 3 capture and release cycles at CCD of 10 mA. For capture (CCD) process, the FDS was reduced to react with CO₂ for 30 min and then rested for 150 min. For release (charge) process, CO₂ adducts (FSCO₂⁻) were oxidized to release CO₂ and regenerate FDS, at 10 mA to 1.35 V followed by a 105 min constant voltage of 1.35 V hold and a 90 min rest. (e) The voltage-capacity curves for capture-release cycles shown in (d). (f) Release/capture efficiency (blue square), CO₂ capacity utilization (yellow circle) and columbic efficiency (green hexagon) for 3 cycles shown in (d).

Note: the other experimental conditions are same as the **Figure 5** one in main text unless otherwise noted.

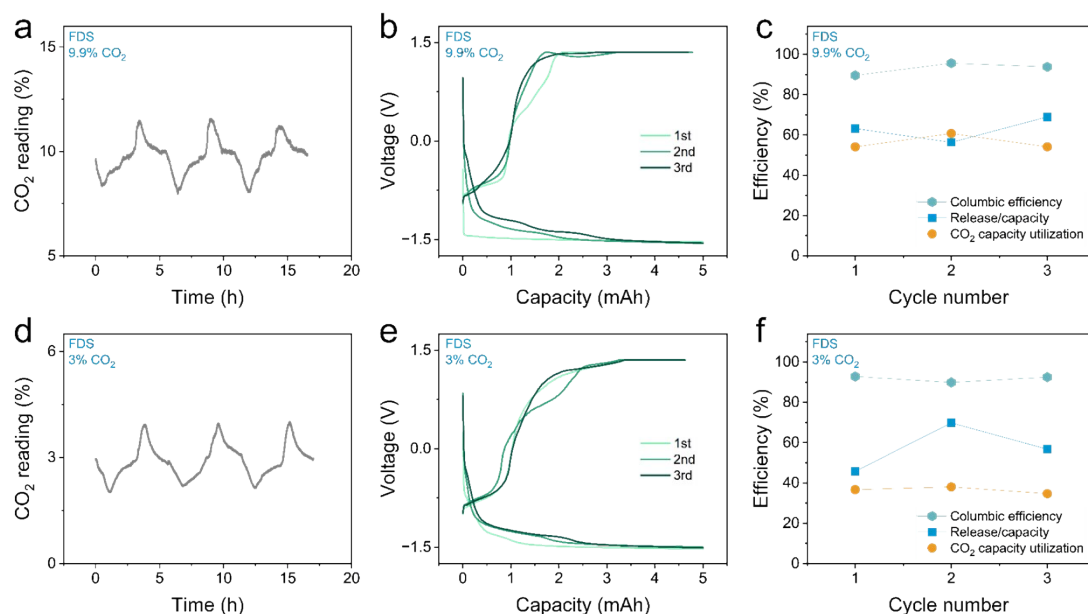


Figure S19. Performance of CO₂ capture and release cycles in a flow cell with FDS under different CO₂ concentration. **(a)** CO₂ readings curves at the gas outlet of FDS tank over 3 capture and release cycles under 9.9% CO₂. For capture (CCD) process, the FDS was reduced to react with CO₂ at 5 mA for 60 min and then rested for 110 min. For release (charge) process, CO₂ adducts (FSCO₂⁻) were oxidized to release CO₂ and regenerate FDS, at 5 mA to 1.35 V followed by a 105 min constant voltage of 1.35 V hold and a 30 min rest. **(b)** The voltage-capacity curves for capture-release cycles shown in **(a)**. **(c)** Release/capture efficiency (blue square), CO₂ capacity utilization (yellow circle) and columbic efficiency (green hexagon) for 3 cycles shown in **(a)**. **(d)** CO₂ readings curves at the gas outlet of FDS tank over 3 capture and release cycles under 3.0% CO₂. For capture (CCD) process, the FDS was reduced to react with CO₂ at 5 mA for 60 min and then rested for 120 min. For release (charge) process, CO₂ adducts (FSCO₂⁻) were oxidized to release CO₂ and regenerate FDS, at 5 mA to 1.35 V followed by an 80 min constant voltage of 1.35 V hold and a 40 min rest. **(e)** The voltage-capacity curves for capture-release cycles shown in **(d)**. **(f)** Release/capture efficiency (blue square), CO₂ capacity utilization (yellow circle) and columbic efficiency (green hexagon) for 3 cycles shown in **(d)**.

Note: the other experimental conditions are same as the **Figure 5** one in main text unless otherwise noted.

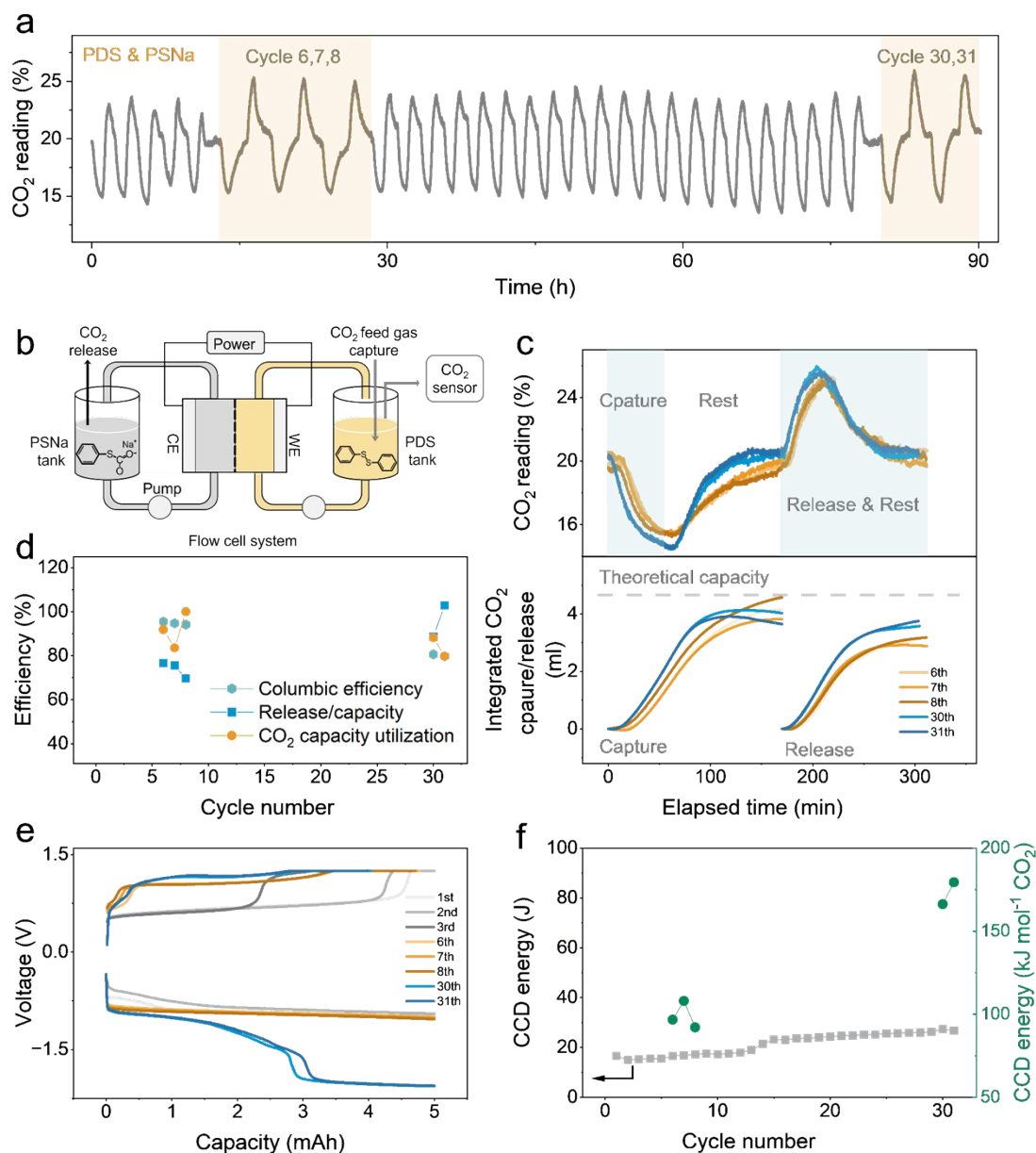


Figure S20. Performance of CO₂ capture and release cycles in a flow cell with PDS and PSNa.

(a) CO₂ readings at the gas outlet of PDS tank over 31 capture and release cycles for ~90 h of operation. Within these cycles, only 6th, 7th, 8th, 30th and 31st cycles include rest processes to calculate the amount of capture/release CO₂.

(b) Schematic drawing of the CO₂ capture-release flow system. The PDS tank filled with PTFE beads was consecutively inputted with 20% CO₂ in N₂ at a flow rate of 2 standard cubic centimeters per minute (sccm), with a CO₂ sensor connected to the gas outlet. The PDS tank contained 5 ml DMF electrolyte with 0.2 M PDS and 0.5 M NaTFSI as the sorbent and supporting electrolyte, respectively. On the opposite side, the sodium phenyl thiolate (PSNa) tank was composed of 10 ml 0.1 M PSNa and 0.5 M NaTFSI. Since the PSNa tank was kept under CO₂ atmosphere, the PSNa will react with CO₂ generating sodium phenyl thiocarbonate (PSCO₂Na). Both liquid electrolytes were flowed through the electrochemical cell (2 × 2 cm² electrode area) at a flow rate of 4 ml min⁻¹. Carbon felts were used as the working electrode (WE) and counter electrode (CE).

(c) The upper one is overlays of selected capture and release cycles from (a) with the indication of capture and release steps by the shaded regions; the one below is the cumulative amount of captured and released CO₂ in selected cycles. For CCD process, the PDS was reduced to react with CO₂ at 5 mA for 60 min and then rested for 110 min. While on the opposite side, the PSCO₂Na was oxidized to release CO₂ and reproduces PDS. For the charge process, CO₂ adducts (PSCO₂⁻) in PDS tank were oxidized to release CO₂ and regenerate PDS, at 5 mA to 1.35 V followed by a 40 min constant voltage of 1.35 V hold and a 60 min rest. In the PSNa tank, the PDS was reduced and then captured CO₂ forming PSCO₂Na again.

(d) Release/capture efficiency (blue square), CO₂ capacity utilization (yellow circle) and Columbic efficiency (green hexagon) for the cycles with rest processes shown in (a).

(e) The voltage-capacity curves for selected capture-release cycles.

(f) The energy consumption of CCD processes through integrating the voltage-capacity curves. CCD energy (gray square) for all cycles, and CCD energy (green circle) for the cycles with rest process.

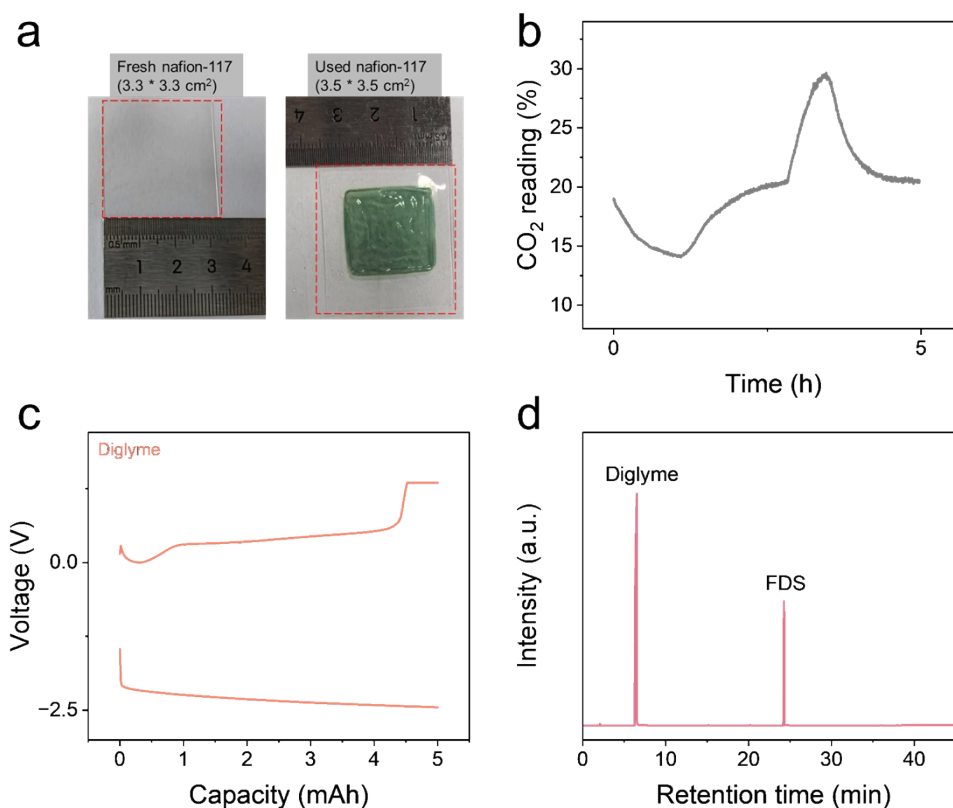


Figure S21. Performance of CO₂ capture and release cycle in a flow cell with FDS by using diglyme as solvent.

(a) photographs showing a piece of fresh nafion membrane (3.3 * 3.3 cm²) and a piece of used nafion membrane (3.5 * 3.5 cm²). The expansion rate of the nafion membrane is about 112.5% after treatment, which is much smaller than that of 186.0% in DMF solvent (**Figure S17**). The smaller expansion rate can help to alleviate the crossover of electrolyte. Thus, in this experiment one membrane was used. There were green substances absorbed on nafion membrane after use. The green substances might be the ferrocene derivatives absorbed on nafion membrane, and they could cause the increase of cell resistance during the cycling experiment.

(b) CO₂ readings at the gas outlet of FDS tank for one capture and release cycle. For capture (discharge) process, the FDS was reduced to react with CO₂ at 5 mA for 60 min and then rested for 110 min. For release (charge) process, CO₂ adducts (FSCO₂⁻) were oxidized to release CO₂ and regenerate FDS, at 5 mA to 1.35 V followed by a 25 min constant voltage of 1.35 V hold and a 50 min rest.

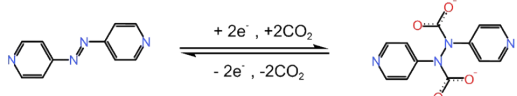
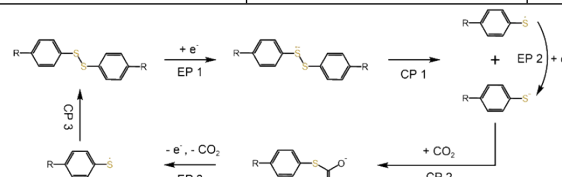
(c) The voltage-capacity curve for CO₂ capture-release cycle shown in (b). The applied voltage was larger than that when using DMF as solvent. That means the ionic conductivity of membrane decrease when using diglyme as solvent, which leads to higher energy consumption.

(d) GC-MS spectra of electrolyte in FDS tank after cyclic experiment. The MS peaks of diglyme and FDS are obvious, and ferrocene derivatives may be too less to be detected. That indicates that the membrane with smaller expansion rate is beneficial to alleviating the crossover problem. Meanwhile, there is not any side product was found, which means that the side reaction between thiolate anion and solvent can be avoided by choosing suitable solvent.

Note: the other experimental conditions are same as the **Figure 5** one in main text unless otherwise specified.

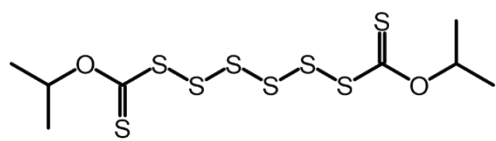
Table S10. Summary of selected redox-active molecules for electrochemical CO₂ capture and release.

Molecule	Estimated theoretical energy consumption (kJ/mol CO ₂)	Demonstrated energy consumption (kJ/mol CO ₂)	Demonstrated system/device	Description/advantage	Ref.
1,8-ESP	—	36-55	Flow system with flow cell	high capture capacity of 0.86-1.41 mol L ⁻¹ and an extremely low degradation rate of <0.01% per day	11
	Mechanism: <p>The mechanism for 1,8-ESP is shown in two parts. On the left, the 'Charge' cycle involves the oxidation of 1,8-ESP (a redox-active molecule with two sulfonic acid groups) to its radical cation (+2 e⁻), which then reacts with CO₂ to form a carbonate species (HCO₃⁻ / CO₃²⁻) and H₂O. On the right, the 'Discharge' cycle involves the reduction of the carbonate species back to CO₂ and OH⁻, while the radical cation of 1,8-ESP is regenerated to its original state (-2 e⁻).</p>				
AQ	—	254-830	Custom-made gas cell	Heterogeneous CO ₂ capture with AQ solid electrode. Perform under pure CO ₂ at 0.1 A g ⁻¹ .	12
PAQ	~34 (Ionic liquid of [Bmim][TF ₂ N])	~40-90	Parallel passage electrochemical cell	Heterogeneous CO ₂ capture with PAQ solid electrode. Performed under 10% CO ₂ at ionic liquid electrolyte with faradic efficiency of 60%-90%	13
TCQ	21.2-34.7 (0.2 M TBAPF ₆ in DMF solutions)	—	H-Cell with glass frit	Performed under 10% CO ₂ with ethanol as additive. Light sensitivity for TCQ.	14
LQ	—	35-220	Continuous flow system with two flow cells	0.1 MPa pure CO ₂ capture and release at current of 0.4-1.4 mA cm ⁻²	2
	Mechanism: <p>The mechanism for LQ shows a redox cycle of a quinone derivative. In the top half, the quinone is reduced to its semiquinone radical anion (+e⁻) and then to its fully reduced hydroquinone form (+e⁻), which captures CO₂. In the bottom half, the hydroquinone is oxidized back to the semiquinone (-e⁻) and then to the quinone (-e⁻), releasing CO₂.</p>				

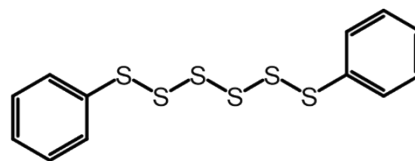
AzPy	~16 (0.1 M TBAPF ₆ in DMSO electrolyte)	120	Flow system with flow cell	Performed under 18.5% CO ₂ + 3% O ₂ at 2 mA cm ⁻² . Only considering energy for CO ₂ capture	3
		156		Performed under 18.5% CO ₂ + 5% O ₂ at 2 mA cm ⁻² . Only considering energy for CO ₂ capture	
Mechanism:					
					
BDS	~200 (Ionic liquid of BMP TFSI)	—	H-Cell with glass frit	Performed under 300 ppm CO ₂ in N ₂ in DMF solution	4
PDS	141 (0.1 M TBAP in DMF electrolyte)	146 (first cycle) 183.7 (average of 19 cycles)	Flow system with flow cell	Performed under 20% CO ₂ at 1.25 mA cm ⁻² . (Only considering energy for CO ₂ capture)	This work
		128 (average of 5 cycles within 31 cycles)		Use CO ₂ adduct as counter electrolyte. Achieve CO ₂ capture and release with a single energy input.	
FDS	133 (0.1 M TBAP in DMF electrolyte)	153 (First cycle) 200 (average of 25 cycle)	Flow system with flow cell	Perform under 20% CO ₂ at 1.25 mA cm ⁻² . (Only considering energy for CO ₂ capture)	
		161 (First cycle) 212 (average of 11 cycle)		Perform under 20% CO ₂ with 0.1 M H ₂ O at 1.25 mA cm ⁻² . (Only considering energy for CO ₂ capture).	
Mechanism:					
					

Abbreviations of molecule in Table S10 are listed below: **1,8-ESP**: 2,2'-(phenazine-1,8-diyl)bis(ethane-1-sulfonate); **AQ**: anthraquinone; **PAQ**: polyanthraquinone; **[Bmim][TF₂N]**: 1-butyl-3-methylimidazolium bis(trifluoromethylsulfonyl)imide **TCQ**: 2,3,5,6-tetrachloro-p-benzoquinone (TCQ); **LQ**: 2,3-Di-(2-(2-methoxyethoxy)ethoxy)-1,4-naphthoquinone **AzPy**: azopyridine; **BDS**: benzyl disulfide; **MP TFSI**: 1-butyl-1-methylpyrrolidinium bis(trifluoromethylsulfonyl)imide **PDS**: phenyl disulfide; **FDS**: 4-fluorophenyl disulfides.

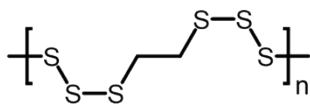
Supplementary Note 1 | potential organodisulfide candidates



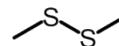
Diisopropyl xanthogen polysulfide (DIXPS)



Phenyl hexasulfide (PHS)



Polyethylene hexasulfide (PEHS)



Dimethyl disulfide (DMDS)

The above show some representative organodisulfides for lithium-sulfur battery. Diisopropyl xanthogen polysulfide (DIXPS) and Phenyl hexasulfide (PHS) are symmetric organopolysulfides.^{15, 16} They could have better electrochemical performance due to their longer sulfur chain, which leads to higher electrochemical activity. However, the insoluble Li_2S is generated during their discharge process. Polyethylene hexasulfide (PEHS) can be used as a solid electrode for heterogeneous CO_2 capture,¹⁷ but it also faces the problem of generating insoluble Li_2S . Dimethyl disulfide (DMDS) with simple structure makes the investigation of its CO_2 capture and release mechanism easy,¹⁸ but its redox performance is difficult to be tuned via molecular engineering due to its simple structure.

Supplementary Note 2 | DFT calculations

The binding energy was obtained from the change of the enthalpy for the binding of thiolate (RS^-) to CO_2 , as the equation below:

$$\Delta H = H_{\text{RSCO}_2^-} - (H_{\text{RS}^-} + H_{\text{CO}_2}) \quad (\text{S1})$$

Where, ΔH is binding energy. $H_{\text{RSCO}_2^-}$, H_{RS^-} and H_{CO_2} are the enthalpy of thiocarbonate (RSCO_2^-), RS^- , and CO_2 , respectively.

The standard redox potentials of different disulfides were calculated by the difference of Gibbs free energies. The equations are as followed:

$$\Delta G = G_{\text{red}} - G_{\text{ox}} \quad (\text{S2})$$

$$E^0 = \Delta G / -e \quad (\text{S3})$$

Where, G_{red} and G_{ox} is the reduction and oxidation state species, respectively. ΔG is the difference between G_{red} and G_{ox} . E^0 is the standard redox potential.

Supplementary Note 3 | calculation of CO_2 binding constant (K_b)

Using the data obtained from cyclic voltammetry is a simple way to calculate K_b of redox active molecule. Specifically, the value of K_b can be determined by the shift in half wave potential as a function of the concentration of CO_2 ($[\text{CO}_2]$, mol L^{-1}).^{19, 20} K_b is the inverse of the dissociation constant. The bigger the K_b value, the greater the binding affinity to CO_2 .

If $K_b > 100$, the Eqn. S4 derived from the Nernst equation should be used as below.

$$E_{1/2}(\text{CO}_2) = E_{1/2}(a) + \frac{RT}{nF} \ln(K_b) + q \frac{RT}{nF} \ln \frac{[\text{CO}_2]}{[\text{C}_0]} \quad (\text{S4})$$

where $E_{1/2}(\text{CO}_2)$ and $E_{1/2}(a)$ are the half wave potential of redox active sorbent in the presence and absence of CO_2 , respectively. q is the number of CO_2 that binds to generated nucleophile, C_0 is the standard concentration (mol L^{-1}).

If the $1 \ll K_b < 100$, the Eqn. S4 should not be used, and the derived Eqn. S5 should be used as follows:

$$E_{1/2}(\text{CO}_2) = E_{1/2}(a) + \frac{RT}{nF} \ln \left(K_b \frac{[\text{CO}_2]}{[\text{C}_0]} + 1 \right) \quad (\text{S5})$$

$$E_{1/2}(\text{CO}_2) - E_{1/2}(a) = \Delta E_{pa} \quad (\text{S6})$$

The reduction peak potential of RS^{\bullet} to RS^- can not be observed due to the intrinsic property of RSSR. Therefore, we estimated the $E_{1/2}$ by E_{pa} minus 30 mV.^{14, 21} As shown in Eqn.(S6), the peak shift of $E_{1/2}$ ($E_{1/2}(\text{CO}_2) - E_{1/2}(a)$) can be estimated by ΔE_{pa} (**Table 1**). The CO_2 concentration in DMF at 25 °C is 0.199 M under 0.1 MPa pressure and the Henry's constant (H_c) is 5.001 $\text{M}^{-1} \text{atm}$.²²

In order to verify whether the above method can be used to calculated the K_b of thiolate anions, we investigated the linear correlation between $E_{1/2}$ and CO_2 concentration. The

$E_{1/2}$ were estimated by E_{pa} minus 30 mV, and the E_{pa} were obtained from CV data of PDS under different CO_2 partial pressures (different CO_2 concentration), as shown in the **Figure S22** below. The linear plot of $E_{1/2}$ vs. $[CO_2]$ shows a good linear correlation between $E_{1/2}$ and CO_2 concentration with a R^2 of 0.9655, which demonstrates that the above method can be used to estimate the K_b of thiolate anions.

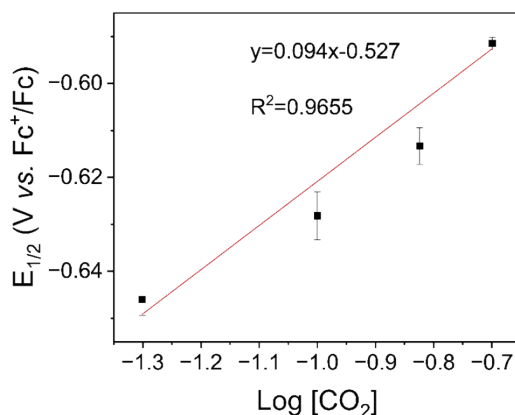


Figure S22. Linear plot of $E_{1/2}$ vs $[CO_2]$ for PDS. The $[CO_2]$ were calculated by Henry's law from different CO_2 partial pressure (25%, 50%, 75% and 100% atm.). The $E_{1/2}$ were estimated by E_{pa} minus 30 mV. The E_{pa} were obtained from CV measurement of PDS under DMF with 0.1 M TBAP.

Supplementary Note 4 | details of chemicals

4-fluorophenyl disulfide (FDS, 98%) was purchased from Thermo Fisher Scientific. Phenyl disulfide (PDS, 98%), Benzyl disulfide (BDS, 98%), Lithium bis(trifluoromethylsulfonylethyl)imide (LiTFSI, 99.5%) were obtained from Meryer. 4-aminodiphenyl disulfide (ADS, 98%+), 2,2'-dipyridinyl disulfide (2-PyDS, 98%+), 4,4'-dipyridinyl disulfide (4-PyDS, 98%), Sodium bis(trifluoromethylsulfonylethyl)imide (NaTFSI, 98%+) and Tetrabutylammonium Perchlorate (TBAP, 99%+) were purchased from Adamas-beta. N, N-Dimethylformamide (99.9%, $H_2O \leq 30$ ppm), Dimethyl sulfoxide (99.9%, $H_2O \leq 50$ ppm) Innochem and 4-[(4-cyanophenyl)disulfanyl] benzonitrile (CDS, 99) were obtained from Innochem. Ferrocene (Fc, 99%) was obtained from D-chem. 4-nitrophenyl disulfide (NDS, 98%) and 4-methylphenyl disulfide (MDS, 98%) were purchased from Crgent Biotech and Energy Chemical, respectively. 4-Methoxyphenyl

disulfide (ODS, 98%) was obtained from Adamas-beta.

References

- (1) Gurkan, B.; Simeon, F.; Hatton, T. A. Quinone Reduction in Ionic Liquids for Electrochemical CO₂ Separation. *ACS Sustainable Chemistry & Engineering* **2015**, *3* (7), 1394-1405. DOI: 10.1021/acssuschemeng.5b00116.
- (2) Diederichsen, K. M.; Liu, Y.; Ozbek, N.; Seo, H.; Hatton, T. A. Toward solvent-free continuous-flow electrochemically mediated carbon capture with high-concentration liquid quinone chemistry. *Joule* **2022**, *6* (1), 221-239. DOI: 10.1016/j.joule.2021.12.001.
- (3) Li, X.; Zhao, X.; Liu, Y.; Hatton, T. A.; Liu, Y. Redox-tunable Lewis bases for electrochemical carbon dioxide capture. *Nature Energy* **2022**, *7* (11), 1065-1075. DOI: 10.1038/s41560-022-01137-z.
- (4) Singh, P.; Rheinhardt, J. H.; Olson, J. Z.; Tarakeshwar, P.; Mujica, V.; Buttry, D. A. Electrochemical Capture and Release of Carbon Dioxide Using a Disulfide-Thiocarbonate Redox Cycle. *J Am Chem Soc* **2017**, *139* (3), 1033-1036. DOI: 10.1021/jacs.6b10806.
- (5) Paparo, A.; Okuda, J. Carbon dioxide complexes: Bonding modes and synthetic methods. *Coordination Chemistry Reviews* **2017**, *334*, 136-149. DOI: 10.1016/j.ccr.2016.06.005.
- (6) Vasudevan, D.; Wendt, H. Electroreduction of oxygen in aprotic media. *Journal of Electroanalytical Chemistry* **1995**, *392* (1-2), 69-74. DOI: 10.1016/0022-0728(95)04044-O.
- (7) Ding, Y.; Chen, Y. P.; Zhang, X.; Chen, L.; Dong, Z.; Jiang, H. L.; Xu, H.; Zhou, H. C. Controlled Intercalation and Chemical Exfoliation of Layered Metal-Organic Frameworks Using a Chemically Labile Intercalating Agent. *J Am Chem Soc* **2017**, *139* (27), 9136-9139. DOI: 10.1021/jacs.7b04829.
- (8) Shen, L.; Qian, Y.; Lyu, Z.; Kim, D.-H.; Kang, D. J. Two-Dimensional Metal-Organic Frameworks and Their Derivative Electrocatalysts for Water Splitting. *Applied Sciences* **2023**, *13* (16). DOI: 10.3390/app13169343.
- (9) Stueber, D.; Patterson, D.; Mayne, C. L.; Orendt, A. M.; Grant, D. M.; Parry, R. W. Carbonates, Thiocarbonates, and the Corresponding Monoalkyl Derivatives. 1. Their Preparation and Isotropic ¹³C NMR Chemical Shifts. *Inorganic Chemistry* **2001**, *40* (8), 1902-1911. DOI: 10.1021/ic0012266.
- (10) Wei, X.; Cosimbescu, L.; Xu, W.; Hu, J. Z.; Vijayakumar, M.; Feng, J.; Hu, M. Y.; Deng, X.; Xiao, J.; Liu, J.; et al. Towards High-Performance Nonaqueous Redox Flow Electrolyte Via Ionic Modification of Active Species. *Advanced Energy Materials* **2014**, *5* (1). DOI: 10.1002/aenm.201400678.
- (11) Pang, S.; Jin, S.; Yang, F.; Alberts, M.; Li, L.; Xi, D.; Gordon, R. G.; Wang, P.; Aziz, M. J.; Ji, Y. A phenazine-based high-capacity and high-stability electrochemical CO₂ capture cell with coupled electricity storage. *Nature Energy* **2023**, *8* (10), 1126-1136. DOI: 10.1038/s41560-023-01347-z.
- (12) Hartley, N. A.; Pugh, S. M.; Xu, Z.; Leong, D. C. Y.; Jaffe, A.; Forse, A. C. Quinone-functionalised carbons as new materials for electrochemical carbon dioxide capture. *Journal of Materials Chemistry A* **2023**, *11* (30), 16221-16232. DOI: 10.1039/d3ta02213g.
- (13) Voskian, S.; Hatton, T. A. Faradaic electro-swing reactive adsorption for CO₂ capture. *Energy & Environmental Science* **2019**, *12* (12), 3530-3547. DOI: 10.1039/c9ee02412c.
- (14) Barlow, J. M.; Yang, J. Y. Oxygen-Stable Electrochemical CO₂ Capture and Concentration with Quinones Using Alcohol Additives. *J Am Chem Soc* **2022**, *144* (31), 14161-14169. DOI: 10.1021/jacs.2c04044.
- (15) Bhargav, A.; Bell, M. E.; Karty, J.; Cui, Y.; Fu, Y. A Class of Organopolysulfides As Liquid Cathode Materials for High-Energy-Density Lithium Batteries. *ACS Applied Materials & Interfaces* **2018**, *10*

- (25), 21084-21090. DOI: 10.1021/acsami.8b06803.
- (16) Bhargav, A.; Manthiram, A. Xanthogen Polysulfides as a New Class of Electrode Material for Rechargeable Batteries. *Advanced Energy Materials* **2020**, *10* (37). DOI: 10.1002/aenm.202001658.
- (17) Bhargav, A.; Chang, C.-H.; Fu, Y.; Manthiram, A. Rationally Designed High-Sulfur-Content Polymeric Cathode Material for Lithium–Sulfur Batteries. *ACS Applied Materials & Interfaces* **2019**, *11* (6), 6136-6142. DOI: 10.1021/acsami.8b21395.
- (18) Chen, S.; Dai, F.; Gordin, M. L.; Yu, Z.; Gao, Y.; Song, J.; Wang, D. Functional Organosulfide Electrolyte Promotes an Alternate Reaction Pathway to Achieve High Performance in Lithium–Sulfur Batteries. *Angewandte Chemie International Edition* **2016**, *55* (13), 4231-4235. DOI: 10.1002/anie.201511830.
- (19) Seo, H. Molecular redox-active organic materials for electrochemical carbon capture. *MRS Communications* **2023**, *13* (6), 994-1008. DOI: 10.1557/s43579-023-00454-y.
- (20) Schmidt, M. H.; Miskelly, G. M.; Lewis, N. S. Effects of redox potential, steric configuration, solvent, and alkali metal cations on the binding of carbon dioxide to cobalt(I) and nickel(I) macrocycles. *Journal of the American Chemical Society* **1990**, *112* (9), 3420–3426. DOI: 10.1021/ja00165a027.
- (21) Elgrishi, N.; Rountree, K. J.; McCarthy, B. D.; Rountree, E. S.; Eisenhart, T. T.; Dempsey, J. L. A Practical Beginner's Guide to Cyclic Voltammetry. *Journal of Chemical Education* **2017**, *95* (2), 197-206. DOI: 10.1021/acs.jchemed.7b00361.
- (22) Gennaro, A.; Isse, A. A.; Vianello, E. Solubility and electrochemical determination of CO₂ in some dipolar aprotic solvents. *Journal of Electroanalytical Chemistry and Interfacial Electrochemistry* **1990**, *289* (1-2), 203-215. DOI: 10.1016/0022-0728(90)87217-8.